Interface effect of Fe and Fe2O3 on the distributions of ion induced defects

Kim, H.; Chancey, M. R.; Chung, T.; Brackenbury, I.; Liedke, M. O.; Butterling, M.; Hirschmann, E.; Wagner, A.; Baldwin, J. K.; Derby, B. K.; Li, N.; Yano, K. H.; Edwards, D. J.; Wang, Y.; Selim, F. A.;

Interface effect of Fe and Fe₂O₃ on the distributions of ion induced defects

Hyosim Kim[1,*], Matthew R. Chancey[1], Thaihang Chung[1,2], Ian Brackenbury[2], Maciej O. Liedke[3], Maik Butterling[3], Eric Hirschmann[3], Andreas Wagner[3], Jon K. Baldwin[4], Ben K. Derby[4], Nan Li[4], Kayla H. Yano[5], Danny J. Edwards[5], Yongqiang Wang[1,4], Farida A. Selim[2,*]

[1]Materials Science and Technology Division, Los Alamos National Laboratory, Los Alamos, NM 87545, USA

[2]Department of Physics and Astronomy, Bowling Green State University, Bowling Green, OH 43403, USA

[3] Institute of Radiation Physics, Helmholtz-Zentrum Dresden-Rossendorf, Bautzner Landstr. 400, 01328 Dresden, Germany.

[4]Center for Integrated Nanotechnologies, Los Alamos National Laboratory, Los Alamos, NM 87545, USA

[5]Energy & Environment Directorate, Pacific Northwest National Laboratory, Richland, WA 99354, USA

*Corresponding Author, email: hkim@lanl.gov (H.K.), faselim@bgsu.edu (F.A.S)

Abstract

The stability of structural materials in extreme nuclear reactor environments—with high temperature, high radiation and corrosive media—directly affects the lifespan of the reactor. In such extreme environments, an oxide layer on the metal surface acts as a passive layer protecting the metal underneath from corrosion. To predict the irradiation effect on the metal layer in these metal/oxide bilayers, nondestructive depth-resolved positron annihilation lifetime spectroscopy (PALS) and complementary transmission electron microscopy (TEM) were used to investigate small-scale defects created by ion irradiation in an epitaxially grown (100) Fe film capped with a 50 nm Fe₂O₃ oxide layer. In this study, the evolution of induced vacancies was monitored, from individual vacancy formation at low doses—10^{-5} dpa—to larger vacancy cluster formation at increasing doses, showing the sensitivity of positron annihilation spectroscopy techniques. Furthermore, PALS measurements reveal how the presence of a metal-oxide interface modifies the distribution of point defects induced by irradiation. TEM measurements show that irradiation induced dislocations at the interface is the mechanism behind the redistribution of point defects causing their accumulation close to the interface. This work demonstrates that the passive oxide layers formed during corrosion impact the distribution and accumulation of radiation induced defects in the metal underneath, and emphasizes that the synergistic impact of radiation and corrosion will differ from their individual impacts.

1. Introduction

Radiation damage in structural materials in extreme reactor environments has been widely studied due to its importance for determining the lifespan of reactors. Materials develop various types of defects under high energy radiation such as vacancies, interstitials, dislocation loops, voids, etc., which degrade materials gradually—especially in the combined extreme environment of high temperatures, high pressures, and a corrosive media [1,2]. In Generation IV (Gen IV) fast reactors, corrosive media such as lead bismuth eutectic (LBE) is expected to be used as a coolant [3]. In such a hostile environment, a thin oxide layer formed on the metal surface protects the surface from corrosion [4]. The most common example of a corrosion resistant alloy using an oxide layer for protection is a stainless steel. The alloying element, Cr, forms Cr_2O_3 on the alloy surface [4-6]. Under certain circumstances, however, the passive oxide layer can break down locally which causes localized corrosion on the exposed metal surface, and radiation can be one of the causes. Despite plenty of literature on irradiation responses of complicated and advanced alloys—such as stainless 304 and 316, A709, T91, HT9 etc., [7-12]—there are only a few fundamental studies conducted on the oxide layer and the base metal under irradiation [13-15], and it is not fully understood how the presence of an oxide layer impacts the evolution of radiation damage. In this study, we particularly focus on the radiation effect on the metal base when capped with an oxide layer in the low radiation dose regime from 10^{-5} to 10^{-2} dpa. For such low dose irradiations, positron annihilation spectroscopy (PAS) is perhaps the only viable tool to detect monovacancy and small vacancy clusters induced by irradiation from a macroscopic scale [16]. Although high resolution annular dark-field scanning transmission electron microscopy (ADF-STEM) may provide atomic scale defect data, the area that can be probed is extremely limited [17]. Therefore, the larger probe area—up to cm^2—of PAS helps to obtain representative data, not dependent on certain grain orientation or local microstructure of the sample. PAS is exceptionally useful for the study of early-stage radiation damage because of its ability to probe individual vacancies with remarkable sensitivity [16].

The recent development of short-pulsed, variable-energy positron beams [18-20] allow us to investigate ion induced defects by depth resolved positron annihilation lifetime spectroscopy (PALS) which can provide detailed information on the change of vacancy clusters' size and density as a function of depth and dose. Such development makes it possible to understand how defect formation and evolution progress within the different layers of material under irradiation, which was not accessible in the past [21]. By recording a birth signal of positrons entering the material and an end signal from positron annihilation in the material, using a short-pulsed positron beam, information about the size and concentration of vacancy like defects can be obtained. Because positrons are implanted and annihilated at different depths, these measurements give insight on the depth distributions of vacancy defects [21-24]. Additionally, combining

PALS and TEM allows us to investigate atomic scale and nanoscale defects and their synergetic impact on radiation damage propagation.

In this study we apply depth resolved PALS and high-resolution transmission electron microscopy (HRTEM) to study how the oxide/metal interface impacts the evolution of ion induced defects in single crystal Fe in the low irradiation damage regime. We also aim to demonstrate the high sensitivity of positron annihilation spectroscopy techniques in probing individual vacancies induced by low doses down to 10^{-5} dpa and illustrate how to calculate the defect densities from PALS measurements by applying the positron trapping models [16].

2. Experimental procedure
2.1. Thin film deposition

The magnetron sputtering system at the Center for Integrated Nanotechnologies (CINT) was utilized to epitaxially grow a 1 µm Fe film (100) on a 1×1 cm^2 MgO (100) substrate, which was capped with a 50 nm thick polycrystalline Fe_2O_3 film [25]. A pure (> 99.99%) Fe target and a hematite-Fe_2O_3 ($\alpha-Fe_2O_3$) target were used for deposition. During the deposition, the base pressure in the chamber was < 6.6×10^{-6} Pa. The substrate was first cleaned using an RF bias of 30 W for 180 s before deposition. For Fe and Fe_2O_3 deposition, the stage was heated up to 500 °C and 600 °C, respectively. This temperature was maintained for 30 mins before the deposition. During the deposition, Ar flow was 30 SCCM (standard cubic centimeters per minute), and the base pressure was maintained at 0.4 Pa. The Fe target was set to 400 W with the DC power supply, and the Fe_2O_3 target to 100 W with the RF power supply, respectively. In addition, the substrate RF bias was tuned to 10 W to enhance surface diffusion during film growth.

2.2. Ion irradiation

Irradiation was conducted at the Ion Beam Materials Laboratory (IBML) in Los Alamos National Laboratory (LANL) and the Ion Beam Laboratory (IBL) in Sandia National Laboratory (SNL) using a 2 MeV Fe^{2+} rastered beam at room temperature. Five identical film specimens were irradiated to 1.0×10^5, 1.0×10^{-4}, 1.0×10^{-3}, 1.0×10^{-2}, and 2.2×10^{-2} displacements-per-atom (dpa), equivalent to 9.1×10^9, 9.1×10^{10}, 9.1×10^{11}, 9.1×10^{12}, and 2.0×10^{13} ions/cm^2 ion fluences, respectively. Stopping and Range of Ions in Matter (SRIM) 2013 code was used to calculate damage profiles with the Kinchin-Pease option [26]. The displacement threshold energies used for the calculations are 40 eV for Fe and 28 eV for O [27]. Fig. 1 shows the dpa and Fe ions (atomic %) profiles of 2.2×10^{-2} peak dpa calculated by SRIM. A 2 MeV Fe ion

beam penetrates through the 50 nm Fe_2O_3 cap and reaches to the end of the 1 μm epitaxially grown Fe film. The peak damage region is located within the Fe film at a depth of ~600 nm from the surface. Note that the damage in the oxide layer is lower compared to the metal layer due to low oxide density.

Due to the single crystal nature of the Fe film, ion channeling was a concern when irradiating at direction normal to the surface of the target. A 2 MeV Fe^{2+} beam irradiation in the single crystal Fe has a half-angle ($\psi_{1/2}$) of ~0.26 degrees, meaning that the beam needs to be well aligned within this small angle in reference to the normal direction to achieve good channeling. In addition, the unavoidable beam de-channeling through the top 50 nm Fe_2O_3 polycrystalline layer makes the channeling probability of 2 MeV Fe beam even less likely and insignificant.
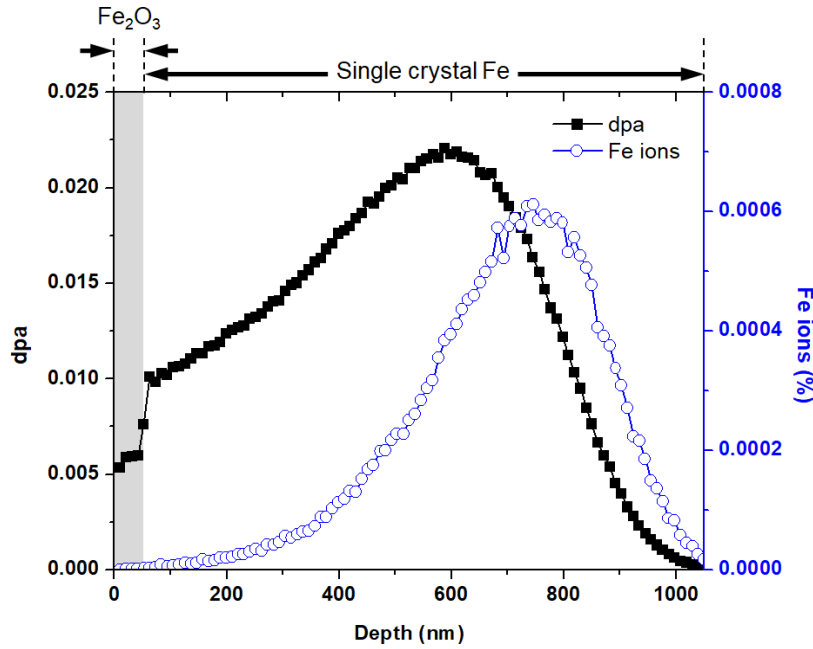

Figure 1 SRIM calculation of Fe_2O_3 (50 nm) capped single crystal Fe film (1μm) specimen irradiated using 2 MeV Fe ions to 2.2×10^{-2} dpa.

2.3. Variable energy positron annihilation lifetime spectroscopy

Variable energy PALS measurements were carried out at the Electron Linac for beams with high Brilliance and low Emittance (ELBE) facility at the Helmholtz-Zentrum Dresden-Rossendorf (HZDR) in Dresden, Germany, using the Monoenergetic Positron Spectroscopy (MePS) beamline with a positron flux of ~10^6/s [20]. PALS spectra were collected using a $CeBr_3$ scintillator detector with a homemade software employing SPDevices ADQ14DC-2X with 14-bit vertical resolution and 2GS/s horizontal resolution and

with a time resolution function of about 0.230 ns [28]. The measurements were performed for incident positron energies between 2-12 keV and a positron lifetime spectrum was collected at each energy. The Makhovian positron implantation profiles at different energies can be found in [16]. All lifetime spectra contained at least 10^7 counts for good statistics. The resolution function applied for spectrum analysis uses two Gaussian functions with distinct intensities depending on the positron implantation energy and appropriate relative shifts. The spectra were deconvoluted using the non-linearly least-squared based package PALSfit fitting software [28] into two or three discrete main lifetime components (the residual components of the relative intensity <1% were omitted from the discussion, as they originated from the surface states or small spectra background inhomogeneities).

Positrons are prone to be trapped by vacancies and other open volume defects as they are repelled by ion cores in the lattice because of their positive charge [16,30]. When they annihilate with electrons, two characteristic 511 keV γ-rays are emitted which can be detected and analyzed to characterize defects in materials. Positrons normally thermalize and diffuse until they become trapped or annihilate at interstitial atomic positions in the absence of defects. Positron trapping at defects leads to a longer lifetime because of a lower electron density at these locations. By measuring the time difference between the birth (positron generation) and death (511 keV annihilation signal) of positrons, a positron lifetime spectrum is generated and analyzed to provide insightful information about the size and density of open volume defects. PALS is indeed the most effective positron technique for defect characterization in terms of type, size, and concentration and it has been successfully used to fully characterize point and complex defects even in complex functional materials [31-35].

Typically, the positron lifetime spectrum consists of exponential decay terms which requires nonlinear fitting procedures as mentioned above, and the result gives lifetime components τ_i and its relative intensity I_i as shown in Eq.1.

$$N(t) = \sum_{i=1}^{k+1} \frac{I_i}{\tau_i} \exp\left(-\frac{t}{\tau_i}\right) \qquad Eq.(1)$$

Here, by comparing the extracted positron lifetime components from the measurements with the positron lifetime values in defect free and defected bulk, we identify the size of vacancies and their change with irradiation and depth. From theory and previous measurements, positron lifetime in defect free bulk Fe is 106-110 ps, while mono-vacancy, di-vacancy, and dislocations in Fe give lifetimes of 175-190 ps, 197 ps, and 165 ps, respectively [16,36]. Lifetime spectra fitting in this study revealed two or three major lifetime components (τ_1, τ_2, and τ_3) with three different intensities (I_1, I_2, and I_3).

2.4. Transmission electron microscopy

The unirradiated reference sample and the 2.2×10^{-2} dpa sample were characterized using an FEI Tecnai F30 field emission transmission electron microscopy (TEM) in the Electron Materials Laboratory (EML) at LANL. A focused ion beam (FIB) lift-out technique was utilized to fabricate cross-sectional $\sim10\times10\,\mu m^2$ TEM foils. The 30 kV Ga beam was used to deposit a Pt layer on the sample to protect the surface and to further etch and polish the foil. Then, an 8 kV Ga beam was used for final cleaning to remove surface damage caused by the high energy Ga beam during foil polishing. For TEM characterization, bright-field (BF) and high-resolution TEM (HRTEM) images were used. Note that the defects smaller than ~1 nm may not be detected due to the resolution limit of the TEM and that the Ga beam may cause contrast degradation during the TEM foil thinning process. HRTEM micrographs were obtained from the interface of the oxide layer and the Fe film of both the reference and the 2.2×10^{-2} dpa samples. The fast-Fourier-transform (FFT) and inverse-FFT (IFFT) images obtained from HRTEM images were used to further characterize the interface.

3. Results and Discussion

3.1. PALS measurements and defect size information

Fig. 2 shows the positron lifetime components and their relative intensities of one pristine and five irradiated samples as a function of positron beam energy and mean positron implantation depth. The location of the interface between the oxide cap and the Fe film is indicated by a black solid line on each graph. Fitting the lifetime spectra returned 2 major lifetime components for the pristine and the 10^{-5} dpa irradiated sample and three lifetime components for the 10^{-4}, 10^{-3}, and 10^{-2} dpa samples. τ_1 is below the bulk lifetime value of Fe in the pristine, 10^{-5}, and 10^{-4} dpa irradiated samples across the film thickness; it represents the reduced bulk lifetime and reflects positron annihilation from Bloch states [16] in the bulk, not from trapping states. In the 10^{-3} and 10^{-2} dpa irradiated samples, τ_1 varies within the depth. It is also below the bulk lifetime except in the layers adjacent to the interface. The interpretation of that will be discussed below. The value of each defect lifetime component was used to identify the vacancy size according to the defect lifetimes in Fe presented in the experimental section and in Table I in Ref.6. By inspecting the lifetime components in Fig. 2, only one defect type is identified in the pristine and 10^{-5} dpa irradiated sample across the measured depth, corresponding to small vacancy clusters with an average size of 3 vacancies (Fig. 2b). It can also be seen from the lifetime intensities (Fig. 2d and 2e) that about 20-30% of positrons annihilated within the bulk and about 70-80% annihilated within these small vacancy clusters. In the irradiated samples with 10^{-4}, 10^{-3}, and 10^{-2} dpa, two defect groups are identified. One corresponding

to small vacancy clusters of less than 10 vacancies (Fig. 2b) and the other corresponding to large vacancy clusters up to 50 vacancies (Fig. 2c). The size and density of these small and large clusters vary with increasing radiation doses and are strongly depth dependent.

The most significant finding in Fig. 2 is the large increase in the defect size and concentration close to the interface which starts to take place at 10^{-4} dpa. τ_1 (Fig. 2a) jumps to 200 ps only in the 30-40 nm adjacent to the metal/oxide interface in the 10^{-3} and 10^{-2} dpa samples and returns to less than 100 ps at deeper depths. This indicates that small vacancy clusters were formed only close to the interface and no positron annihilates within the bulk in this region. τ_2 (Fig. 2b) also jumps from 200 ps to 300~350 ps in the same layers adjacent to the interface in the 10^{-3} and 10^{-2} dpa, respectively, and returns to 200 ps at deeper depths. Furthermore, large vacancy clusters/voids are formed in these adjacent layers to the interface in the 10^{-2} and 10^{-3} dpa. Fig. 1 shows that the peak damage induced by irradiation is about 600 nm, ~550 nm away from the interface. This indicates that the presence of the metal/oxide interface modifies the distributions of ion induced defects and their size and concentrations. However, for the higher irradiation dose of 0.02 dpa, there is no distinguishable region close to the interface, and the depth dependence of ion induced defects is aligned with the dpa profile as it seems to increase at higher depths.
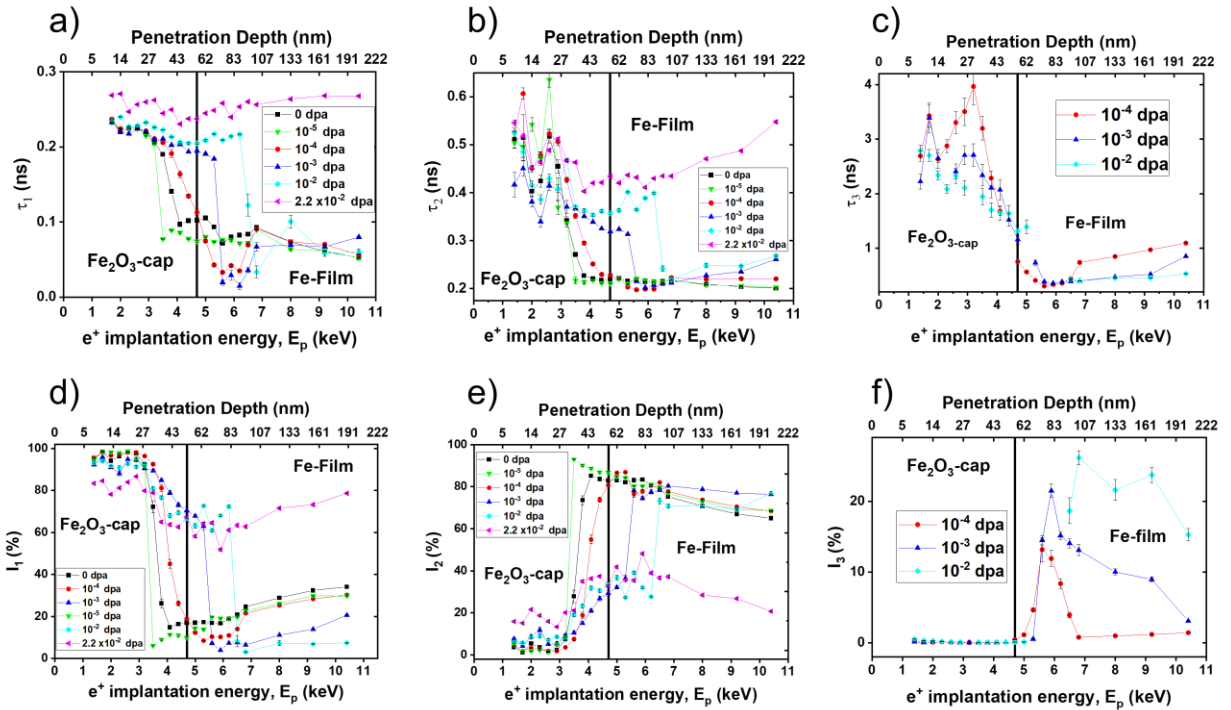

Figure 2 PALS measurements of Fe films capped with oxide layers as a function of positron beam energy and average penetration depth before and after irradiation. (a-c) Lifetime components τ_1, τ_2, and τ_3 and

(d-f) corresponding intensities. All the error bars are included in these graphs, however most of them are smaller than the symbols.

3.2. Defect density calculations

A goal of this study is to calculate the density of each defect group in the metal layer for this low dose irradiation regime. For that, the positron trapping model [16, 37] was applied to calculate the defect density from PALS measurements. The model assumes that one or more types of defects are present and homogenously distributed in the medium trap positrons. Each defect type leads to a characteristic positron lifetime. For the pristine sample and the 10^{-5} dpa irradiated sample, only one defect type is extracted from their lifetime spectra and the positron trapping rate, K_d, was calculated using the following equation:

$$K_d = \frac{I_2}{I_1}\left(\frac{1}{\tau_B} - \frac{1}{\tau_D}\right) \qquad\qquad Eq.\,(2)$$

where τ_B and τ_D are the bulk and defect lifetimes, respectively, and I_1 and I_2 are their measured intensities. For irradiated samples with 10^{-4}, 10^{-3}, and 10^{-2} dpa, their lifetime measurements indicated the presence of two dominant defect groups. Thus, the two trapping rates, K_1 and K_2, for each defect group were calculated from the following two equations:

$$K_1 = \frac{I_2 I_3(\lambda_{D1} - \lambda_{D2}) + I_2(\lambda_B - \lambda_{D1})}{1 - I_2 - I_3} \qquad\qquad Eq.\,(3)$$

, and

$$K_2 = \frac{I_2 I_3(\lambda_{D2} - \lambda_{D1}) + I_3(\lambda_B - \lambda_{D2})}{1 - I_2 - I_3} \qquad\qquad Eq.\,(4)$$

where λ_B and λ_D are the annihilation rates for the bulk and defect lifetime (the reciprocal of the bulk and defect lifetime, respectively) and I_2 and I_3 are the measured intensities for the defect lifetimes τ_2 and τ_3, respectively. Figure 3 depicts the trapping rate for each defect group as a function of dose and depth.

Then the density of each defect group was calculated from the trapping rate as follows:

$$\rho_d = \frac{K_d}{\eta_0} \qquad\qquad Eq.\,(5)$$

where η_0 is the trapping coefficient (specific trapping rate for each defect type) which is known for Fe from theory and experiments [21] and plotted in Fig. 3. Note that the assumption was made that the specific trapping rate is independent of the cluster size.

It should be mentioned that in this study, we only focused on investigating radiation induced defects in the metal layer and we did not perform any analysis on the oxide layer. This is because the lifetime of defects in Fe_2O_3 is not known, thus it is not possible to calculate the defect densities from PALS measurements at present. Note that the missing data points of 10^{-2} dpa between 5 and 6.5 keV in Fig. 3 resulted from positron beam issues during data collection.

In Fig. 4 we presented the size and density of both small vacancy clusters and large vacancy clusters in 3D graphs and their associated 2D maps to illustrate the size, density, and depth distributions of ion induced defects in the Fe films. It should be noted that for the sample irradiated to 0.02 dpa, we presented the PALS measurements in Fig. 2. However, it is not possible to calculate the defect density in this sample using the trapping model because of the saturation of positron trapping. This can be seen from the absence of lifetime component below the bulk lifetime in Fe in this sample (Fig. 2a).
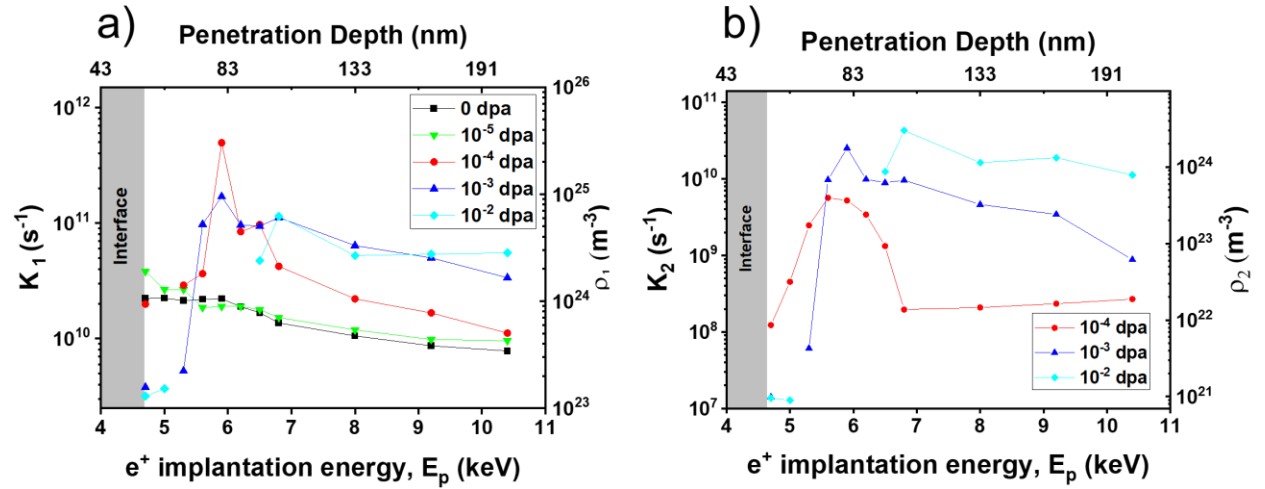
Figure 3 Positron trapping rate in the metal layer for (a) small vacancy clusters (K1) and (b) large vacancy clusters (K2) as a function of dose and depth. Calculated densities of small and large vacancy clusters are also shown on the right Y-axes in each figure.
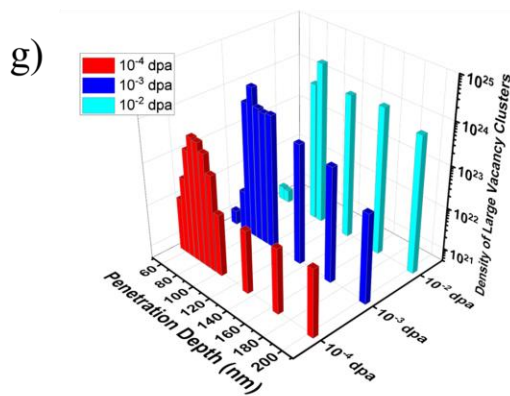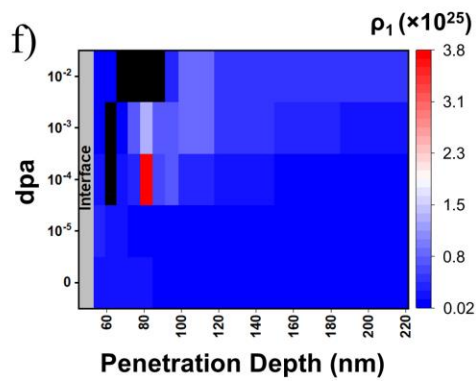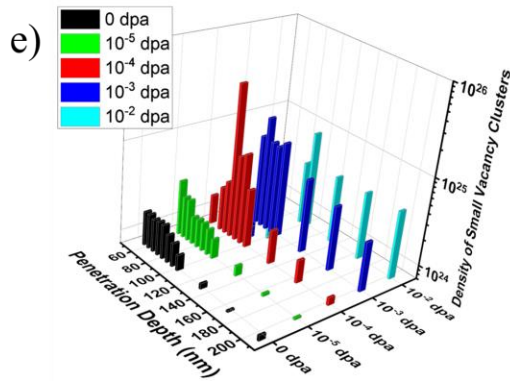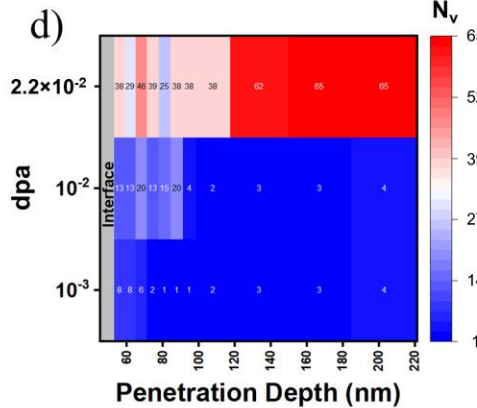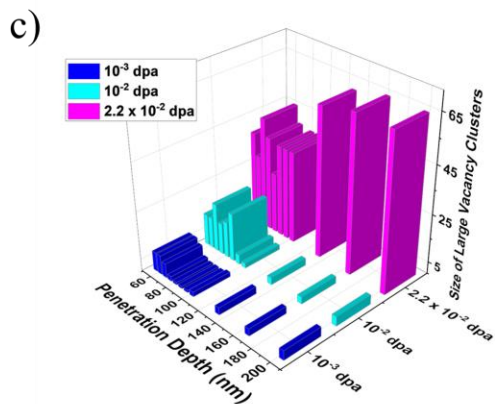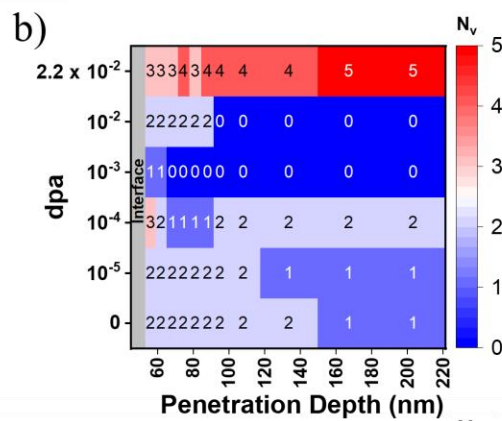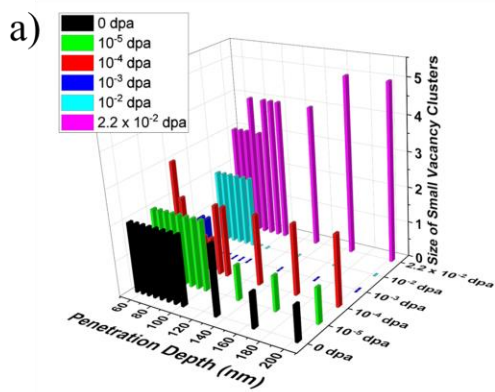
9
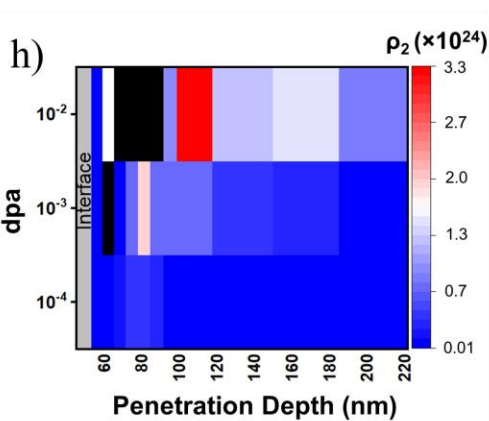
Figure 4 3D representation of the size distributions along with their corresponding heat maps of (a,b) small vacancy clusters, (c,d) large vacancy clusters. Large vacancy clusters did not form with dpa less than 10^{-4} dpa. 3D representation of defect density distributions along with their corresponding heat maps of (e,f) small and (g,h) large vacancy clusters. The black regions in (f) and (h) represent missing data points.

3.3. TEM results on pristine and 2.2×10^{-2} dpa samples

TEM micrographs were obtained from the pristine sample and the irradiated sample (2.2×10^{-2} dpa) to investigate film morphologies and defect characteristics. TEM BF low magnification images in Fig. 5a and 5b confirm the polycrystalline structure of the Fe_2O_3 oxide layers and the single crystallinity of the Fe films. Note that these images were obtained from the different tilting conditions, which gives different contrast in the Fe and the MgO substrate. The thicknesses of the oxide layer and the Fe film were measured as ~50 nm and ~1 μm, respectively. HRTEM images were obtained from the interfaces of the oxide layer and the Fe film from each sample and presented in Fig. 5c and 5d. Both HRTEM images were obtained from the same orientation for comparison. Moiré pattern is observed at the pristine sample interface caused by an interference of diffracting crystal lattice planes that are overlapping with two different spacings or orientations. The irradiated sample did not show any Moiré pattern at the interface as shown in Fig. 5d,

instead it showed a disturbance in lattice continuity caused by irradiation. The differences in those interfaces are shown in detail in Fig. 6.
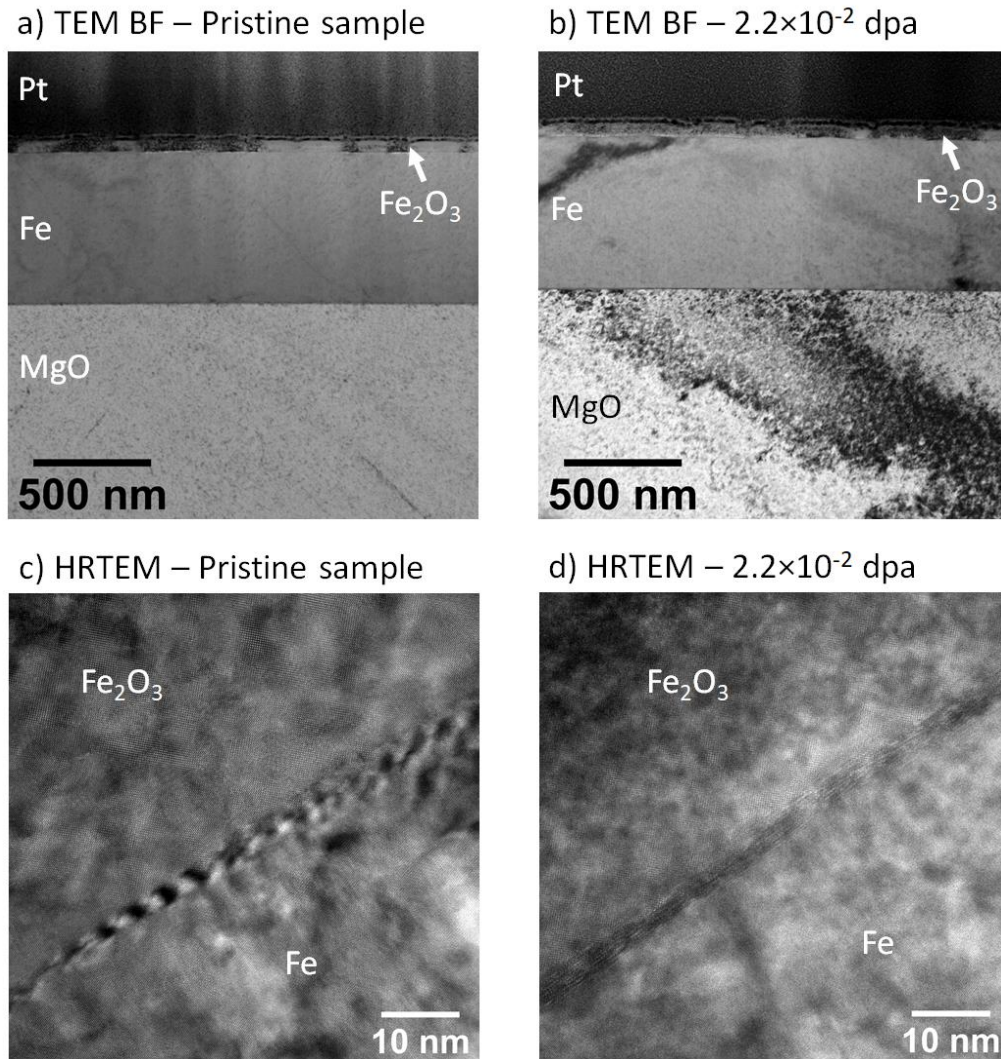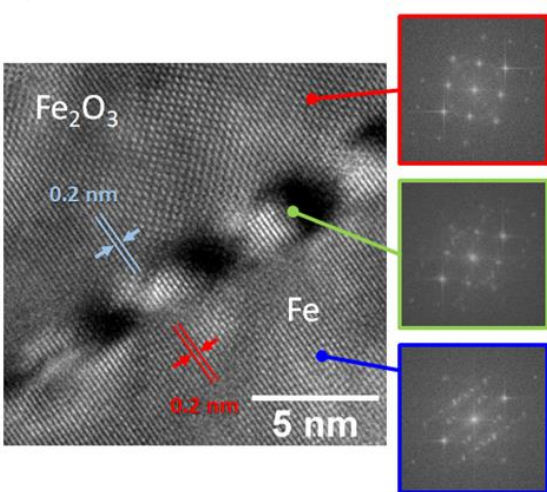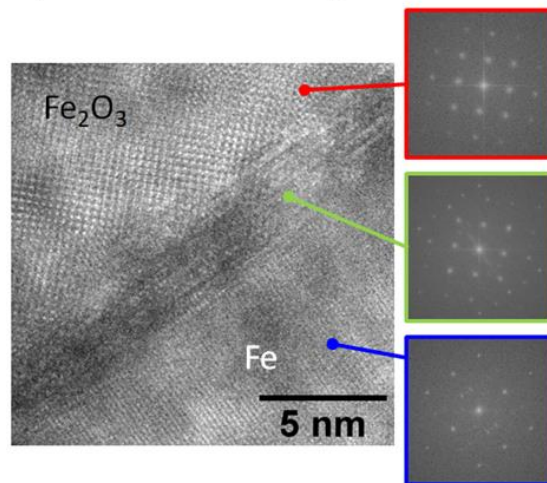

Figure 5 TEM BF and HRTEM micrographs of pristine and 2.2×10^{-2} dpa irradiated samples. (a,b) TEM BF low magnification images show the sample morphologies, and oxide layers show polycrystalline structure. (c,d) HRTEM images of pristine and irradiated oxide and Fe film interfaces show lattice misfits and radiation damage, respectively.
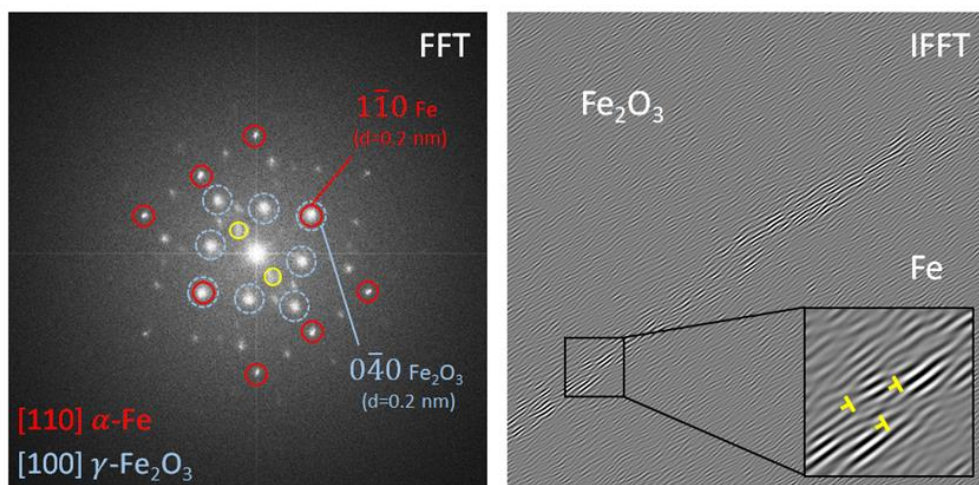
a) HRTEM – Pristine sample

b) HRTEM – 2.2×10^{-2} dpa

c) FFT and IFFT images of 2.2×10^{-2} dpa sample

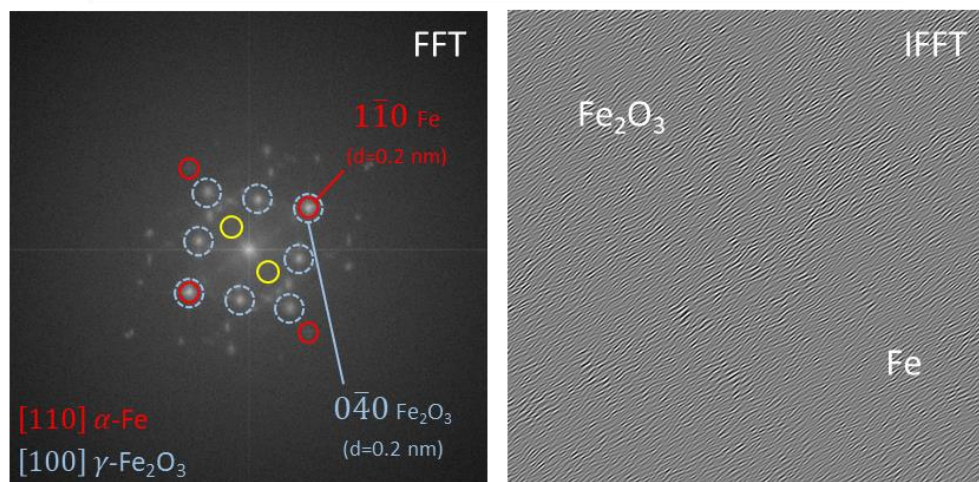d) FFT and IFFT images of pristine sample

13

Figure 6 HRTEM micrographs of the pristine and the irradiated samples. (a) Interface of the pristine sample with FFT images obtained from each region, (b) interface of the irradiated sample with FFT images obtained from each region, and (c) FFT and IFFT images of the irradiated sample. FFT patterns used to generate IFFT image are marked with yellow circles in the FFT image. Lattice parameters of Fe $1\bar{1}0$ and γ-Fe$_2$O$_3$ $0\bar{4}0$ are the same as 0.2 nm, and those planes are aligned. IFFT image from yellow circled patterns show dislocation developments caused by irradiation. (d) FFT and IFFT images of the pristine sample. FFT patterns used to generate IFF image are marked with yellow circles. No patterns were observed within the yellow circle, and corresponding IFFT image also did not reveal dislocation features like the irradiated sample.

Fig. 6a and 6b provide magnified HRTEM images of each sample to show details of the interface morphologies with FFT images obtained from each region. Both TEM images were taken at the same orientation, [100] for γ-Fe$_2$O$_3$ and [110] for Fe for comparison. Fig. 6c provides an FFT image obtained from the irradiated sample. The red solid circles are the FFT patterns from Fe, and the blue dashed circles are the FFT patterns from γ-Fe$_2$O$_3$. Both the $1\bar{1}0$ plane of Fe and the $0\bar{4}0$ plane of γ-Fe$_2$O$_3$ have ~0.2 nm lattice distances and are aligned with each other in the FFT image. The Fe and Fe$_2$O$_3$ have a cube-on-edge orientation relationship [38]. It is also possible to observe the alignment of those two planes in Fig. 6a through the interface. The FFT patterns marked with yellow circles, that do not belong to either Fe or Fe$_2$O$_3$, were used to generate the IFFT image. The IFFT image reveals dislocation development at the interface under irradiation (Fig. 6c), and this was not shown in the pristine sample (Fig. 6d). FFT patterns shown in the yellow circles of Fig. 6c are not shown in the pristine sample FFT image (Fig. 6d), and only background was reconstructed in the IFFT image. No voids were observed after the highest dose. The small vacancy clusters detected by PALS were not detectable in the TEM image due to the resolution limit of the TEM.

Dislocations are important point defect sinks in crystalline materials, and they act as biased sinks for interstitials or interstitial clusters, which is the fundamental cause of void formation [39]. The order of the preferential absorption of interstitials over vacancies varies in each material system. For example, bias for interstitial is on the order of 0.1-0.2 in austenitic stainless steels, which means 10-20 more interstitials are incorporated into the dislocations than vacancies, when 100 interstitials and vacancies are produced by irradiation [39].

At low dose (10^{-5} dpa), the low level of defect formation and the Fe and Fe$_2$O$_3$ layer boundary—which acts as a neutral defect sink—help the recombination of radiation induced defects. Consequently, PALS result did not show any significant amount of vacancy accumulation in Fe near the interface.

With increasing doses, formation of radiation induced dislocations at the interface observed by TEM suggests stronger preferential absorption of interstitials, and the vacancy accumulation was observed accordingly in PALS as shown in Fig. 3. The vacancy cluster density in Fig. 3 shows three distinctive

behaviors along the irradiation depth. Near the interface (50~65 nm depth), vacancy cluster densities are consistently low, and this is due to the defect recombination effect at the boundary. At a slightly deeper depth (~80 nm), where the vacancy cluster density peaks, the radiation induced dislocations at the interface cause a stronger effect and interstitials with higher mobility are preferentially absorbed leaving the vacancies behind. As a result, high vacancy cluster densities are shown at deeper depth. Further into the material (>100 nm), no fluctuation in vacancy cluster density is observed, as no boundary or dislocation effects are in place. Instead, vacancy cluster density progressively increases with the increasing dose. Therefore, based on TEM and PALS results, it can be concluded that irradiation induced dislocations at the interface are responsible for the redistribution and accumulation of small point defects next to the interface and the increase in their size.

4. Conclusions

In this study, the evolution of radiation induced vacancies was monitored, from individual vacancy formation at low doses—10^{-5} dpa—to larger vacancy cluster formation at increasing doses, showing the sensitivity of PAS techniques. One- and two-defect trapping models were applied to calculate the density of the two dominant defect groups induced by irradiation. Most importantly, PALS measurements revealed the strong impact of the metal/oxide interface on the distribution of ion induced defects. It is interesting to observe the increase in vacancy size and density next to the interface, even though the interface was ~550 nm from the peak damage region. The TEM results revealed the film morphologies at the Fe_2O_3 and Fe interface before and after irradiation, and the HRTEM showed radiation induced dislocations at the interface. This is most likely responsible for the accumulation of point defects close to the interface, and the result was explained by two different defect sink effects—interface as a neutral defect sink and dislocations as preferential interstitial sinks. The study sheds light on defect evolution under ion irradiation with increasing dose in the metal/oxide interface which has not been adequately studied in this field. The metal/oxide interface is a very important passive layer that protects the metal from corrosion. For the nuclear reactor core materials, radiation damage is also an inevitable material degrading factor along with corrosion. It is important to understand how the oxide layer and the metal below react under irradiation, and how it affects the corrosion process. To that end, this work demonstrates that a passive oxide layer can modify the distribution of radiation induced defects and their accumulation, which can further affect the corrosion.

Acknowledgements

References

1. S.J. Zinkle, G.S. Was, Materials challenges in nuclear energy, Acta Mater. 61 (2013) 735-758.
2. S.J. Zinkle, J.T. Busby, Structural materials for fission & fusion energy, Mater. Today 12 (2009) 12-19.
3. F. Schmidt, P. Hosemann, R.O. Scarlat, D.K. Schreiber, J.R. Scully, B.P. Uberuaga, Effects of radiation-induced defects on corrosion, Annu. Rev. Mater. Res. 51 (2021) 293-328.
4. L. Ma, F. Wiame, V. Maurice, P. Marcus, Origin of nanoscale heterogeneity in the surface protecting stainless steel against corrosion, Mater. Degrad. 3 (2019) 29.
5. N. Wint, D.J. Warren, A.C.A. DeVooys, H.N. McMurray, The use of chromium and chromium (III) oxide PVD coatings to resist the corrosion driven coating delamination of organically coated packaging steel, J. Electrochem. Soc. 167 (2020) 141506.
6. T. Jonsson, S. Karlsson, H. Hooshyar, M. Sattari, J. Liske, J.-E. Svensson, L.-G. Johansson, Oxidation after breakdown of the chromium-rich scale on stainless steels at high temperature: Internal oxidation, Oxid. Met. 85 (2016) 509-536.
7. B.H. Sencer, G.S. Was, M. Sagisaka, Y. Isobe, G.M. Bond, F.A. Garner, Proton irradiation emulation of PWR neutron damage microstructures in solution annealed 304 and cold-worked 316 stainless steels, J. Nucl. Mater. 323 (2003) 18-28.
8. H. Kim, J.G. Gigax, J. Fan, F.A. Garner, T.-L. Sham, L. Shao, Swelling resistance of advanced austenitic alloy A709 and its comparison with 316 stainless steel at high damage levels, J. Nucl. Mater. 527 (2019) 151818.

9. J.G. Gigax, T. Chen, H. Kim, J. Wang, L.M. Price, E. Aydogan, S.A. Maloy, D.K. Schreiber, M.B. Toloczko, F.A. Garner, L. Shao, Radiation response of alloy T91 at damage levels up to 1000 peak dpa, J. Nucl. Mater. 482 (2016) 257-265.

10. H. Kim, J.G. Gigax, C.J. Rietema, O. El Atwani, M.R. Chancey, J.K. Baldwin, Y. Wang, S.A. Maloy, Void swelling of conventional and composition engineered HT9 alloys after high-dose self-ion irradiation, J. Nucl. Mater. 560 (2022) 153492.

11. Y. Chen, Irradiation effects of HT-9 martensitic steel, Nucl. Eng. Tech. 45 (2013) 311-322.

12. C. Cabet, F. Dalle, E. Gaganidze, J. Henry, H. Tanigawa, Ferritic-martensitic steels for fission and fusion applications, J. Nucl. Mater. 523 (2019) 510-537.

13. K.H. Yano, A.A. Kohnert, A. Banerjee, D.J. Edwards, E.F. Holby, T.C. Kaspar, H. Kim, T.G. Lach, S.D. Taylor, Y.Q. Wang, B.P. Uberuaga, D.K. Schreiber, Radiation-enhanced anion transport in hematite, Chem. Mater. 33 (2021) 2307-2318.

14. K.H. Yano, A.A. Kohnert, T.C. Kaspar, S.D. Taylor, S.R. Spurgeon, H. Kim, Y. Wang, B.P. Uberuaga, D.K. Schreiber, Radiation enhanced anion diffusion in chromia, J. Phys. Chem. C 125 (50) (2021) 27820-27827.

15. K.H. Yano, A.A. Kohnert, T.C. Kaspar, S.D. Taylor, S.R. Spurgeon, H. Kim, Y. Wang, D.K. Schreiber, Influence of irradiation-induced defects on anion transport in epitaxial Cr_2O_3, Microscopy and Microanalysis 27 (S1) (2021) 2904.

16. F.A. Selim, Positron annihilation spectroscopy of defects in nuclear and irradiated materials – a review, Mater. Char. 174 (2021) 110952.

17. J. Hong, Z. Hu. M. Probert, K. Li, D. Lv, X. Yang, L. Gu, N. Mao, Q. Feng, L. Xie, J. Zhang, D. Wu, Z. Zhang, C. Jin, W. Ji, X. Zhang, J. Yuan, Z. Zhang, Exploring atomic defects in molybdenum disulphide monolayers, Nat. Commun. 6 (2015) 6293.

18. W. Egger, P. Sperr, G. Kögel, G. Dollinger, Pulsed low energy positron system (PLEPS) at the Munich research reactor FRM II, Phys. Status Solidi. C 4 (2007) 3969-3972.

19. K. Ito, Preliminary results on low-energy positron age-momentum correlation measurements based on a radioisotope-source positron beam, JJAP Conf. Proc. 7 (2018) 011302.

20. A. Wagner, M. Butterling, M.O. Liedke, K. Potzger, R. Krause-Rehberg, Positron annihilation lifetime and Doppler broadening spectroscopy at the ELBE facility, AIP Conf. Proc. 1970 (2018) 040003.

21. S. Agarwal, M.O. Liedke, A. Jones, E. Reed, A.A. Kohnert, B.P. Uberuaga, Y.Q. Wang, J. Cooper, D. Kaoumi, N. Li, R. Auguste, P. Hosemann, L. Capolungo, D.J. Edwards, M. Butterling, E. Hirschmann, A. Wagner, F.A. Selim, A new mechanism for void-cascade

interaction from nondestructive depth-resolved atomic-scale measurements of ion irradiation-induced defects in Fe, Sci. Adv. 6 (2020) eaba8437.

22. P. Saadatkia, S. Agarwal, A. Hernandez, E. Reed, I.D. Brackenbury, C.L. Codding, M.O. Liedke, M. Butterling, A. Wagner, F.A. Selim, Point and extended defects in heteroepitaxial β-Ga_2O_3 films, Phys. Rev. Mater. 4 (2020) 104602.

23. M.M. Islam, M.O. Liedke, D. Winarski, M. Butterling, A. Wagner, P. Hosemann, Y. Wang, B. Uberuaga, F.A. Selim, Chemical manipulation of hydrogen induced high p-type and n-type conductivity in Ga_2O_3, Sci. Rep. 10 (2020) 6134.

24. Kršjak, Vladimír, Petr Hruška, Jarmila Degmová, Stanislav Sojak, Pavol Noga, Tielong Shen, Veronika Sabelová, Werner Egger, and Vladimír Slugeň, A new approach to near-surface positron annihilation analysis of ion irradiated ferritic alloys, Nanoscale Adv. 3 (2021) 6596-6607.

25. B. Derby, J. Cooper, T. Lach, E. Martinez, H. Kim, J.K. Baldwin, D. Kaoumi, D.J. Edwards, D.K. Schreiber, B.P. Uberuaga, N. Li, A pathway to synthesizing single-crystal Fe and FeCr films, Surf. Coat. Technol. 403 (2020) 126346.

26. R.E. Stoller, M.B. Toloczko, G.S. Was, A.G. Certain, S. Dwaraknath, F.A. Garner, On the use of SRIM for computing radiation damage exposure, Nucl. Instrum. Methods. Phys. Res. B 310 (2013) 75-80.

27. ASTM E521-96, "Practice for Neutron Radiation Damage Simulation by Charged-Particle Irradiation," ASTM International, West Conshohocken, PA, 1996.

28. 1.Hirschmann, E., M. Butterling, U. Hernandez Acosta, M. O. Liedke, A. G. Attallah, P. Petring, M. Görler, R. Krause-Rehberg, and A. Wagner. "A new system for real-time data acquisition and pulse parameterization for digital positron annihilation lifetime spectrometers with high repetition rates." *Journal of Instrumentation* 16, no. 08 (2021): P0800

29. J.V. Olsen, P. Kirkegaard, N.J. Pedersen, M. Eldrup, PALSfit: A new program for the evaluation of positron lifetime spectra, Phys. Status Solidi. 4 (2007) 4004–4006.

30. F.A. Selim, D.P. Wells, J.F. Harmon, J. Kwofie, G. Erikson, T. Roney, New positron annihilation spectroscopy techniques for thick materials, Radiation Physics and Chemistry 68, Issues 3-4 (2003) 427-430.

31. D.J. Keeble, S. Wicklein, R. Dittmann, L. Ravelli, R.A. Mackie, W. Egger, Identification of A- and B-site cation vacancy defects in perovskite oxide thin films, Phys. Rev. Lett. 105 (2010) 226102.

32. L. Zhang, J. Wu, P. Stepanov, M. Haseman, T. Zhou, D. Winarski, P. Saadatkia, S. Agarwal, F. A. Selim, H. Yang, Q. Zhang, Y. Wang, C. Wong, H. Chen, Defects and solarization in YAG transparent ceramics, Photonics Research 7 (2019) 549-557.

33. F.A. Selim, D. Winarski, C.R. Varney, M.C. Tarun, J. Ji, M.D. McCluskey, Generation and characterization of point defects in $SrTiO_3$ and $Y_3Al_5O_{12}$, Results Phys. 5 (2015) 28–31.

34. de Rojas, Julius, Alberto Quintana, Aitor Lopeandía, Joaquín Salguero, Beatriz Muñiz, Fatima Ibrahim, Mairbek Chshiev et al. "Voltage-driven motion of nitrogen ions: a new paradigm for magneto-ionics." *Nature communications* 11, no. 1 (2020): 1-8.

35. Quintana, Alberto, Enric Menéndez, Maciej O. Liedke, Maik Butterling, Andreas Wagner, Veronica Sireus, Pau Torruella et al. "Voltage-controlled ON–OFF ferromagnetism at room temperature in a single metal oxide film." *ACS nano* 12, no. 10 (2018): 10291-10300.

36. M.J. Puska, R.M. Nieminen, Defect spectroscopy with positrons: A general calculational method, J. Phys. F 13 (1983) 333–346.

37. M. Eldrup, B.N. Singh, Studies of defects and defect agglomerates by positron annihilation spectroscopy, J. Nucl. Mater. 251 (1997) 132-138.

38. L. Yang, Y. Jiang, Y. Wu, G.R. Odette, Z. Zhou, Z. Lu, The ferrite/oxide interface and helium management in nano-structured ferritic alloys from the first principles, Acta Mater. 103 (2016) 474-482.

39. W.G. Wolfer, The dislocation bias, J. Computer-Aided Mater. Des. 14 (2007) 403–417.